



Hydrogen-assisted phase transition in a trihydride MgNi_2H_3 synthesized at high H_2 pressures: Thermodynamics, crystallographic and electronic structures

V.A. Yartys,^{a,*} V.E. Antonov,^b A.I. Beskrovnyy,^c J.-C. Crivello,^d R.V. Denys,^a V.K. Fedotov,^b M. Gupta,^e V.I. Kulakov,^b M.A. Kuzovnikov,^{b,1} M. Latroche,^d Yu.G. Morozov,^f S.G. Sheverev^c and B.P. Tarasov^g

^aInstitute for Energy Technology, Kjeller, Norway

^bInstitute of Solid State Physics RAS, Chernogolovka, Russia

^cFrank Laboratory of Neutron Physics, JINR, Dubna, Russia

^dInstitut de Chimie et des Matériaux Paris-Est, ICMPE, CNRS-UPEC, Thiais, France

^eThermodynamique et Physico-Chimie d'Hydrides et Oxydes, Université Paris Sud, Orsay, France

^fInstitute of Structural Macrokinetics and Materials Science RAS, Chernogolovka, Russia

^gInstitute of Problems of Chemical Physics RAS, Chernogolovka, Russia

Received 27 July 2014; revised 1 September 2014; accepted 7 September 2014

Abstract— MgNi_2 intermetallic was synthesized by powder metallurgy and crystallizes with a Laves-type $C36$ structure (space group $P6_3/mmc$ (No. 194); $a = 4.826$; $c = 15.832$ Å). At 300 °C during interaction with hydrogen (deuterium) gas compressed to 2.8–7.4 GPa, a trihydride $\text{MgNi}_2\text{H}(\text{D})_{3.2}$ was synthesized. The trihydride remained metastable at ambient conditions allowing its structure, stability and magnetic properties to be studied. The formation of $\text{MgNi}_2\text{H}_{3.2}$ is associated with a complete rebuilding of the initial hexagonal structure into the orthorhombic distorted MoSi_2 -type sublattice (space group $Fmmm$ (No. 69); $a = 4.55$; $b = 4.69$; $c = 8.80$ Å). Neutron diffraction of the $\text{MgNi}_2\text{D}_{3.2}$ demonstrated that D atoms fill sites having octahedral Mg_4Ni_2 ($D1/4b$) and planar Ni_2 ($D2/8f$) coordination. Within the framework of the density functional theory, density of states (DOS) calculations showed the formation of a structure around -10 to -6 eV caused by the chemical bonds of hydrogen and its $1s$ states mainly via interaction with the $3d$ states of Ni. Analysis of the electronic structure revealed a charge transfer from Mg to Ni, and to the H atoms. The calculated enthalpy of formation of MgNi_2H_3 is about -30 kJ/mol- H_2 , which is consistent with the stability of the hydride at normal conditions. The initial sample contained a small amount of a secondary MgNi_3 intermetallic, which has been formed during the equilibrium interaction of magnesium and nickel at 800 °C. Thus this compound should be included in the phase diagram of the Mg–Ni system. MgNi_3 decomposes under high-temperature/high-pressure hydrogenation conditions and forms nickel monohydride.

© 2014 Acta Materialia Inc. Published by Elsevier Ltd. All rights reserved.

Keywords: Metal hydrides; Crystal structure; High pressures; Neutron diffraction; DFT

1. Introduction

Magnesium-based alloys and composite materials containing magnesium dihydride (MgH_2) are important hydrogen and energy storage materials. Compared to the individual MgH_2 hydride, binary and ternary Ni-containing hydrogen storage alloys of magnesium demonstrate significantly improved rates of hydrogen charge and discharge that mean they can operate at lower temperatures while

maintaining a high hydrogen storage capacity. The beneficial effect of nickel has been demonstrated for a variety of compositions and is caused by the following phenomena: (i) formation of Mg_2NiH_4 containing 3.6 wt.% H and having significantly lower working temperatures (0.1 MPa H_2 at 223 °C) for the reversible absorption and desorption of hydrogen as compared to MgH_2 [1]; (ii) nickel solubility in Mg-rich La–Mg alloys such as $\text{La}_2\text{Mg}_{17}$ takes place on both La and Mg sites to form $\text{La}_{1.80}\text{Ni}_{0.40}\text{Mg}_{16.73}\text{Ni}_{0.27}$ and, when the alloy is prepared in a nanostructured state, this results in the reversibility of H absorption–desorption and extremely fast kinetics of the processes of H exchange in the alloy [2]; (iii) substitution of La by Mg allows a fine tuning of the thermodynamic properties of the ternary La–Mg–Ni alloys and their hydrides, making them suitable for applications as anodes for advanced Ni-metal hydride batteries.

* Corresponding author. Address: Norwegian University of Science and Technology, Trondheim, Norway. Fax: +47 63 81 29 05; e-mail: volodymyr.yartys@ife.no

¹ Present address: Institute of Physical Chemistry PAS, Warsaw, Poland.

These include hydrides of the $\text{La}_{1.5}\text{Mg}_{0.5}\text{Ni}_7$ alloy formed on the basis of La_2Ni_7 [3] and $\text{La}_{3-x}\text{Mg}_x\text{Ni}_9$ -based hydrides ($x = 0-2$) with the hydrogen dissociation pressure increasing 1000-fold following an increase in the Mg concentration from $x = 0$ in LaNi_3 to $x = 2$ in LaMg_2Ni_9 [4]. The La_2MgNi_9 alloy corresponding to $x = 1$ has the best properties as battery anode material with the discharge capacity reaching 400 mAh g^{-1} [5,6]. Hydrogen sublattice in $\text{La}_2\text{MgNi}_9\text{D}_{13}$ shows local ordering of H atoms around Mg and Ni and can be built from the MgH_6 octahedra and NiH_4 tetrahedra [7].

The alloy with the highest content of magnesium, LaMg_2Ni_9 , has a structure composed of two building blocks with the stoichiometry LaNi_5 and MgNi_2 . The corresponding deuteride $\text{LaMg}_2\text{Ni}_9\text{D}_{9.5}$ was synthesized at 950 bar D_2 [8] and showed hydrogenation properties dramatically different from those for LaNi_3 . While LaNi_3 is prone to hydrogen-induced disproportionation, the Mg-containing intermetallic reversibly forms a hydride with $\Delta H_{\text{des}} = -24.0 \text{ kJ/mol-H}_2$ and an equilibrium pressure of H_2 desorption of 18 bar at 20°C . A pronounced hysteresis of H_2 absorption and desorption is evidenced by a high value of H_2 absorption pressure, ~ 100 bar higher than for desorption. The observed values of hydrogen capacities cannot be explained solely by hydrogen insertion into the LaNi_5 slabs, and require hydrogen incorporation into the MgNi_2 fragments of the structure to reach the experimentally observed H/M ratios. This clearly shows an influence of the LaNi_5 layer in the stacking structures on the hydrogenation of the MgNi_2 slabs, which for the individual MgNi_2 compound is achieved only at several kbar of H_2 . Thus, LaNi_5 -assisted hydrogenation of MgNi_2 in the LaMg_2Ni_9 hybrid structure takes place. Indeed, in the $\text{LaMg}_2\text{Ni}_9\text{D}_{9.5}$ ($a = 5.21-5.26$; $c = 25.81-25.85 \text{ \AA}$), D atoms are accommodated in both Laves and CaCu_5 -type slabs. In the LaNi_5 CaCu_5 -type layer, D atoms fill three types of interstices: a deformed octahedron [La_2Ni_4], and [$\text{La}(\text{Mg})_2\text{Ni}_2$] and [Ni_4] tetrahedra, to yield $\text{LaNi}_5\text{D}_{5.7}$ composition. The D distribution is very similar to that in the individual $\beta\text{-LaNi}_5\text{D}_{5.9}$ deuteride. The overall chemical composition $\text{LaMg}_2\text{Ni}_9\text{H}_{9.5}$ can be presented as $\text{LaNi}_5\text{H}_{5.7} + 2\text{MgNi}_2\text{H}_{1.9}$. This indicates that the hydrogenation of the MgNi_2 slab proceeds under rather mild H_2/D_2 pressure conditions; the equilibrium D_2 desorption pressure is just 20 bar D_2 . The refinements showed a partial filling by D atoms of four types of the tetrahedral interstices in the MgNi_2 slab; these include two types of the available [MgNi_3] and two types of the [Mg_2Ni_2] tetrahedra.

After Mg_2Ni , the second intermetallic compound formed in the Mg–Ni binary system is MgNi_2 [9,10]. Individual MgNi_2 intermetallic alloy crystallizes with a C36 Laves-type structure [9,10]. Hydrogenation of MgNi_2 was achieved by Okada et al. at hydrogen pressures of 2–5 GPa and temperatures of $700-800^\circ\text{C}$ [11,12]. Exposing mixtures of Mg and Ni powders containing 65–70 at.% Ni to these conditions gave single-phase samples with a nearly invariable hydrogen/metal atomic ratio of ~ 1.07 [11]. In the case of the nearly stoichiometric MgNi_2 composition (67 at.% Ni) this ratio corresponded to the formula $\text{MgNi}_2\text{H}_{3.2}$ and to a hydrogen concentration of 2.23 wt.%. The hydrides with < 67 at.% Ni had a body-centered tetragonal metal lattice, and the crystal structure of those with > 67 at.% Ni was orthorhombic [11]. The hydrides $\text{MgNi}_2\text{H}_{3.2}$ with $x = 67$ at.% Ni could have either a tetragonal metal lattice (space group $I4/mmm$ (No. 139),

$a = 3.27(3)$; $c = 8.78(9) \text{ \AA}$) [11] or an orthorhombic one ($a = 4.60$; $b = 4.68$; $c = 8.78 \text{ \AA}$) [12]. Both the tetragonal and orthorhombic hydrides decomposed in a single decomposition step at 190°C with an enthalpy change of 30.6 kJ/mol-H_2 [11,12].

In the present paper, powder samples of the orthorhombic hydride $\text{MgNi}_2\text{H}_{3.2}$ and deuteride $\text{MgNi}_2\text{D}_{3.2}$ are synthesized under a high hydrogen (deuterium) pressure and the crystal structure of the metal lattices of both samples are examined by X-ray diffraction; the positions of the D atoms in the structure of $\text{MgNi}_2\text{D}_{3.2}$ are determined by neutron diffraction. This experimental work is supplemented by magnetization measurements and ab initio calculations of the equilibrium crystal structure of the MgNi_2H_3 hydride, its electronic structure and its thermodynamics.

2. Experimental details

The starting MgNi_2 material was prepared from high-purity Mg (99.8 %; 44 mcm) and Ni (99.995 %; 150 mcm) powders mixed in a slightly overstoichiometric ratio 1:2, with an Mg excess of 2 wt.%, and compacted by pressing up to $1.47 \times 10^3 \text{ MPa}$ into pellets with a diameter of 15 mm. The obtained pellets were sintered in argon gas at 800°C for 12 h and quenched into ice water after annealing.

To prepare the $\text{MgNi}_2\text{-H}$ hydride, $\sim 100 \text{ mg}$ MgNi_2 were powdered in an agate mortar and loaded with hydrogen by a 24 h exposure to a H_2 pressure of 7.4 GPa at 300°C in a high-pressure cell. The synthesized sample was subsequently rapidly cooled to 100 K. The hydrogenation method is described in more detail elsewhere [14]. The experiment was carried out in a toroidal high-pressure chamber [13] using AlH_3 as an internal hydrogen source. The synthesized $\text{MgNi}_2\text{-H}$ sample was then stored in liquid nitrogen to prevent hydrogen loss and oxidation by air.

A 1000 mg sample of the $\text{MgNi}_2\text{-D}$ deuteride was prepared in a similar way by a 24 h exposure of powdered MgNi_2 to a D_2 pressure of 2.8 GPa at 300°C . In this case, the high-pressure chamber was of the “lentil” type [13] and the deuterium gas was produced in the high-pressure cell by thermal decomposition of AlD_3 . In view of the small protium concentration $\text{H}/(\text{H} + \text{D}) = 2.9(2) \text{ at.}\%$ in the AlD_3 used [15], we neglected H contamination of the obtained $\text{MgNi}_2\text{-D}$ sample in the analysis of its neutron diffraction pattern.

The thermal stability and the total hydrogen (deuterium) content of the samples were determined by hot extraction into a pre-evacuated calibrated volume, which involved heating the sample from -186 to 660°C at a rate of $20^\circ\text{C min}^{-1}$. The mass of the analyzed probe was a few milligrams. The method is described in more detail in Ref. [16].

The virgin MgNi_2 powder was examined by X-ray diffraction (XRD) at room temperature with a Siemens D500 diffractometer using monochromated $\text{Cu } K_{\alpha 1}$ radiation. The hydrogenated and deuterated samples were studied by XRD at 85 K with a Siemens D500 diffractometer using $\text{Cu } K_{\alpha}$ radiation selected by a diffracted beam monochromator. The diffractometer was equipped with a home-designed nitrogen cryostat that permitted the powder samples to be loaded without any intermediate warming. The obtained diffraction patterns were analyzed using GSAS [17] and POWDERCELL2.4 software.

The neutron diffraction study of the MgNi₂-D sample was carried out with the time-of-flight (TOF) DN-2 diffractometer installed on the IBR-2M pulsed nuclear reactor at the Joint Institute for Nuclear Research in Dubna, Russia. The sample environment included a vanadium container and a closed-cycle helium refrigerator. The TOF patterns were recorded by a ³He gas-filled proportional detector positioned at the scattering angle $2\theta = 150^\circ$. The background from the sample environment was measured under the same conditions and subtracted from the TOF patterns. The patterns were normalized to the incoherent scattering spectrum of vanadium and the measuring time. Rietveld refinements of the neutron powder diffraction pattern were performed using VISUAL MRIA software [17].

The amount of magnetic impurities in the samples was additionally estimated by measuring their magnetization, σ , with a vibrating sample magnetometer (EG&G PARC M-4500). The $\sigma(H)$ curves were measured at two temperatures, 82 and 295 K, with the magnetic field, H , varying from +10 to −10 kOe and backward at a constant rate of 1.2 kOe min^{−1}.

3. Results and discussion

3.1. The starting MgNi₂ alloy

The XRD pattern of the powdered virgin MgNi₂ alloy is presented in Fig. 1. Profile analysis of this pattern showed that Laves-type MgNi₂ intermetallic compound constituted >90% of the sample. The sample contained also a few wt.% of three minor phases, Ni, MgNi₃ and MgO (see Table 1 for further details). The crystallographic parameters of the hexagonal crystal structure of the MgNi₂ compound (space group $P6_3/mmc$ (No. 194), $a = 4.82565(6)$, $c = 15.8323(3)$ Å)

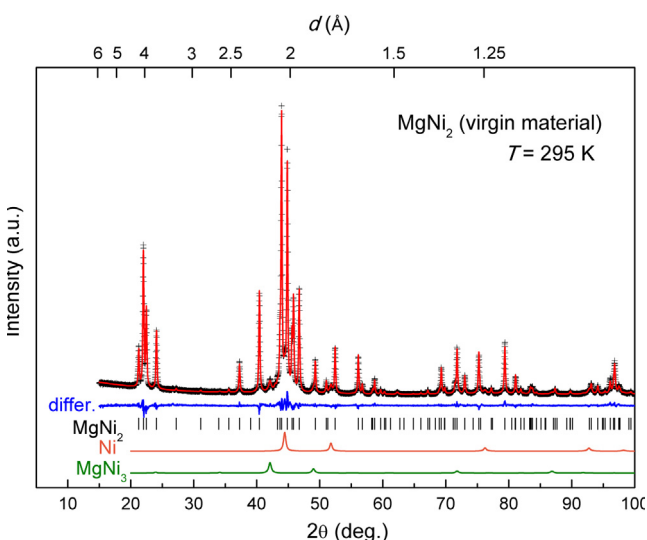


Fig. 1. Profile refinements of the XRD pattern of the starting MgNi₂ alloy. The calculated contribution of the MgNi₃ and Ni impurities (two bottom lines), and the difference “differ.” between the calculated and experimental profiles (line labeled “differ.”) are shown together with experimental points (+) and calculated profiles. Note that MgO impurity is not shown because of a very weak contribution to the overall diffraction pattern (however, it was included into the refinements). Room temperature, Cu $K_{\alpha 1}$ radiation. $R_{wp} = 6.8\%$, $R_p = 5.3\%$, $\chi^2 = 2.6$.

well agree with the reference data [10]. The lattice parameters of the impurities (Ni: face-centered cubic lattice; $a = 3.5301(3)$ Å and MgO: space group $Fm\bar{3}m$ (No. 225); $a = 4.212(1)$ Å) were also found to be very close to the literature data [18,19]. One unexpected minor constituent is the cubic MgNi₃ compound with a Cu₃Au-type structure (space group $Fm\bar{3}m$ (No. 225); $a = 3.7163(3)$ Å). This compound has not yet been presented on the phase diagram of the Mg–Ni system [9]. Recently, it was synthesized by ball milling of a mixture of Mg and Ni metals [20] and considered as a metastable phase. In the present work, the formation of MgNi₃ resulting from the sintering of Mg and Ni at $T = 800^\circ\text{C}$ suggests that this compound should be an equilibrium phase at such a temperature.

3.2. Magnetic properties of the MgNi₂ alloy

The MgNi₂ compound is paramagnetic down to 4 K [21], whereas Ni metal is a ferromagnet with a rather high Curie temperature $T_C = 631$ K (358 °C) [22], and this allows a more accurate estimation of the Ni content in our samples by using magnetization measurements.

The magnetization measurements for the starting MgNi₂ alloy were performed at temperatures significantly lower than the Curie temperature of Ni. At these temperatures of 82 and 295 K, according to the measurements of Ref. [22], the magnetization of the bulk samples of Ni metal reaches saturation, σ_S , in fields below 4 kOe and it does not further change in fields up to 19 kOe. The noticeable increase in the magnetization of our sample at $H > 4$ kOe is a characteristic feature showing the presence of small ferromagnetic Ni particles. The magnetization of such particles should linearly depend on $1/H$ in the high magnetic fields approaching σ_S at $1/H \rightarrow 0$ (e.g. [23]). As one can see from the inset in Fig. 2, the experimental $\sigma(1/H)$ dependences for the MgNi₂ alloy are approximately linear at $1/H < 0.25$ kOe^{−1} (i.e. at $H > 4$ kOe). An extrapolation to $1/H = 0$ (dashed lines in the inset) gives $\sigma_S^{\text{exp}}(82\text{ K}) = 1.66$ emu g^{−1} and $\sigma_S^{\text{exp}}(295\text{ K}) = 1.56$ emu g^{−1}. These values do not differ much from the corresponding values of the magnetization at $H = 10$ kOe, inspiring confidence in the adopted extrapolation procedure.

A comparison of the two obtained σ_S^{exp} values with the values of $\sigma_S^{\text{Ni}}(82\text{ K}) = 58.27$ emu g^{−1} and $\sigma_S^{\text{Ni}}(295\text{ K}) = 54.98$ emu g^{−1} for bulk Ni metal determined in Ref. [22] gives converging results for the concentration x_{Ni} of the Ni amount, i.e. $\sigma_S^{\text{exp}}(82\text{ K})/\sigma_S^{\text{Ni}}(82\text{ K}) = 2.84$ wt.% Ni and $\sigma_S^{\text{exp}}(295\text{ K})/\sigma_S^{\text{Ni}}(295\text{ K}) = 2.84$ wt.% Ni. This value agrees well with independent refinements of the XRD data where the Ni content was found to be 4.6(1) wt.% (see Fig. 1).

The good agreement of the ratio of $\sigma_S^{\text{exp}}(295\text{ K})/\sigma_S^{\text{exp}}(82\text{ K}) = 0.94(1)$ with the precise value of $\sigma_S^{\text{Ni}}(295\text{ K})/\sigma_S^{\text{Ni}}(82\text{ K}) = 0.944$ from Ref. [22] indicates that the Curie temperature of the Ni particles in the MgNi₂ alloy studied in the present work is close to that of bulk Ni metal. Together with the agreement between the estimates of the content of Ni metal resulting from the σ_S^{exp} values and from XRD, this suggests that the magnetization of the starting alloy should solely be due to the Ni minor phase. Consequently, the MgNi₃ secondary phase (as well as the main MgNi₂ phase [21]) is not ferromagnetically ordered at $T \geq 82$ K.

The MgNi₂ compound is known to have a nearly stoichiometric composition at room temperature and only shows a rather narrow interval of mutual solubility of the

Table 1. Crystallographic data for MgNi₂ from the profile refinements of the X-ray powder diffraction presented in Fig. 1. $R_{wp} = 6.8\%$, $R_p = 5.3\%$, $\chi^2 = 2.6$. MgNi₂ (content in the sample 90.1(1) wt.%): space group $P6_3/mmc$; $a = 4.82565(6)$; $c = 15.8323(3)$ Å; $V = 319.290(6)$ Å³.

Atom	Site	X	Y	Z	Ui/Ui* 100
Mg	4e	0	0	0.0943(3)	1.00
Mg	4f	1/3	2/3	0.8443(4)	1.00
Ni	6g	1/2	0	0	1.00
Ni	6h	0.1645(2)	2x	1/4	1.00
Ni	4f	1/3	2/3	0.1253(2)	1.00

Secondary phases present in the sample.

Ni: space group $Fm\bar{3}m$ (No. 225); 4.6(1) wt.%; $a = 3.5301(3)$ Å; $V = 43.99(2)$ Å³.

MgNi₃: space group $Fm\bar{3}m$ (No. 225); 2.9(1) wt.%; $a = 3.7163(3)$ Å; $V = 51.32(3)$ Å³.

MgO: space group $Fm\bar{3}m$ (No. 225); 2.4(2) wt.%; $a = 4.212(1)$ Å; $V = 74.71(8)$ Å³.

components at higher temperatures, the limiting concentration of Ni reaching ~ 67.1 at.% at 800 °C [9]. As the studied MgNi₂ alloy was sintered from Mg and Ni taken in the atomic proportion slightly exceeding 1:2, the extra Ni found in this alloy could only be present as a result of evaporation of more volatile Mg in the course of sintering and further 12 h homogenization annealing at 800 °C. We could thus expect that the annealed MgNi₂ compound would contain ~ 67.1 at.% Ni, characteristic of its equilibrium with the Ni metal.

3.3. The MgNi₂-H sample

High-pressure hydrogenation resulted in the formation of the trihydride MgNi₂H_{3.2}. The sample loaded with hydrogen at 7.4 GPa and 300 °C and quenched to liquid N₂ temperature had a metallic appearance.

Fig. 3 presents an XRD pattern of the “as-quenched” sample. A profile analysis of this pattern showed that the sample consisted of an orthorhombic phase very similar to the MgNi₂H_{3.2} hydride described in Ref. [12] and a few per cent of the fcc nickel hydride. The data also show that the sample contained an unidentified hydride phase.

Let us consider the NiH phase first. Under the conditions of high-pressure synthesis, the nickel contained in the starting MgNi₂ alloy should have formed a monohydride NiH with a cubic NaCl-type structure (space group $Fm\bar{3}m$, $a = 3.740$ Å) [14]. The presence of such a phase with

$a = 3.734(2)$ Å in the MgNi₂-H sample can easily be judged by the isolated (200) line at $2\theta \approx 48.7^\circ$ in the experimental diffraction pattern in Fig. 3.

Studies of the thermal desorption of hydrogen from the quenched MgNi₂-H sample showed that the NiH hydride rapidly decomposes at temperatures near $T = 0$ °C producing a step in the curve of hydrogen desorption (see Fig. 4). At room temperature, the decomposition of NiH is accomplished in just a few minutes. The remaining MgNi₂H_x hydride is thermally stable at room temperature and shows no detectable loss of hydrogen over a period of days. X-ray examination of the sample exposed to room temperature for 3 h gave a diffraction pattern very similar to that presented in Fig. 3 except that the peaks of fcc Ni with $a = 3.52(1)$ Å replaced those of NiH.

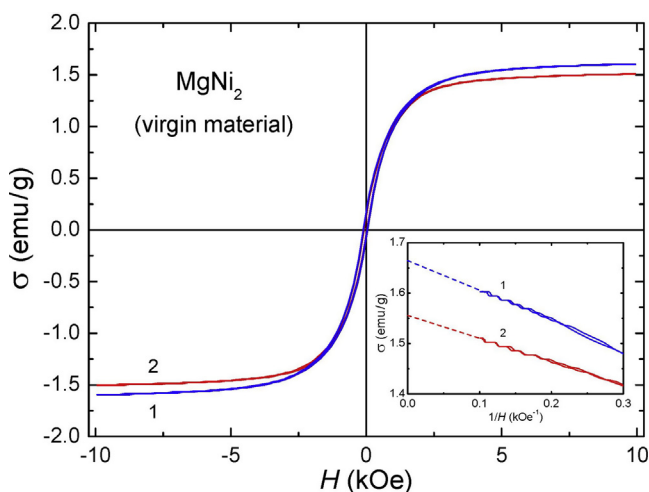


Fig. 2. Magnetization, σ , of a 20 mg sample of the pristine MgNi₂ alloy as a function of magnetic field, H , at $T = 82$ K (curve 1) and 295 K (curve 2). The dashed lines in the inset show linear extrapolations of the experimental $\sigma(1/H)$ plots to $1/H = 0$.

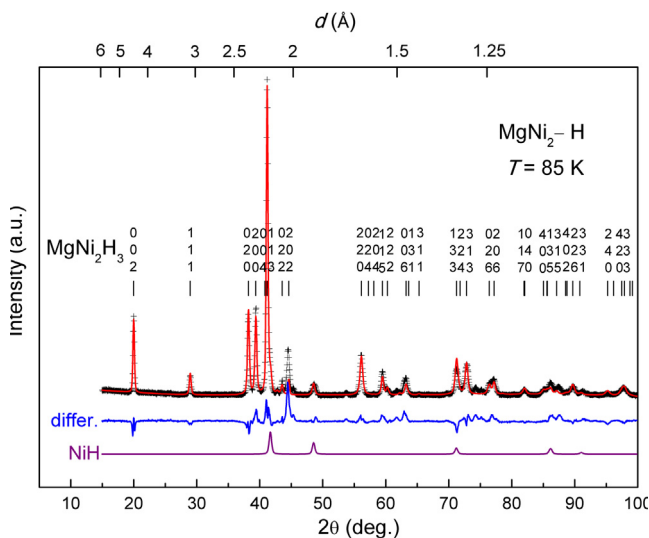


Fig. 3. XRD pattern of the MgNi₂-H sample prepared at a hydrogen pressure of 7.4 GPa and a temperature of 300 °C (upper curve), the calculated contribution from the Ni minor phase (bottom curve) and the difference between the calculated and experimental profiles (the curve labeled “differ.”). A small contribution from the hexagonal ice condensed onto the sample surface while loading it into the nitrogen cryostat is subtracted from the experimental pattern in order to more easily visualize the peaks from the unidentified phase. The measurement conditions are $T = 85$ K, Cu $K_{\alpha 1+\alpha 2}$ radiation. Note that MgO impurity is not shown because of its very weak peak contribution. The constituent phases are: MgNi₂H_{3.2}; 90.7(2) wt.%; space group $Fm\bar{3}m$; $a = 4.551(1)$; $b = 4.684(1)$; $c = 8.793(2)$ Å, $V = 187.42(4)$ Å³. NiH: 7.2(4) wt.%; $a = 3.734(2)$ Å, $V = 52.05(8)$ Å³. MgO: 2.1(5) wt.%; $a = 4.204(9)$ Å, $V = 74.3(4)$ Å³. $R_{wp} = 21.9\%$, $R_p = 15.6\%$, $\chi^2 = 21.5$. The diffraction contribution from ice and from AlH₃ which appeared in the sample because of the applied synthesis and sample handling conditions were subtracted from the XRD pattern.

As seen from Fig. 4, the MgNi_2H_x phase starts decomposing on heating at 100–120 °C. The decomposition of the tetragonal and orthorhombic hydrides $\text{MgNi}_2\text{H}_{3.2}$ synthesized in Refs. [11,12] started at a considerably higher temperature of ~ 190 °C. A possible explanation of the higher thermal stability of the hydrides in Ref. [11,12] is that they were synthesized at much higher temperatures (700–800 °C) and their chemical reaction with the debris of the high-pressure cell could produce a surface layer, forming a barrier to hydrogen diffusion. The black color of the hydrides synthesized in Refs. [11,12] compared to the metallic appearance of our samples can serve as indirect evidence of the existence of such a layer.

A comparison of the desorption curves for the “as-quenched” $\text{MgNi}_2\text{-H}$ sample and that with the NiH phase completely decomposed by a preliminary exposure of the sample to room temperature for 3 h shows that the exposure resulted in the release of ~ 0.15 wt.% H. At the same time, the NiH phase formed by 3 wt.% of the initial Ni phase could only evolve ~ 0.05 wt.% H, which is approximately 3 times less. To accurately determine the amount of NiH in the $\text{MgNi}_2\text{-H}$ sample, we measured its magnetization in the “as-quenched” state and after the 3 h exposure to room temperature. The obtained $\sigma(H)$ dependences are presented in Fig. 5.

The “as-quenched” sample was measured only at $T = 82$ K in order to avoid losses of hydrogen from the NiH phase at higher temperatures. The $\sigma(H)$ dependence of this sample (curve 1 in Fig. 5) forms a hysteresis loop characteristic of a magnetically ordered material. Since NiH is neither ferromagnetic nor superconducting down to $T = 0.3$ K [24], the observed magnetization could be attributed to a certain amount of unreacted Ni (which is most likely), or to the MgNi_2H_x hydride (its magnetic properties have yet not been studied), or to the unidentified impurities. In any case, the magnetization is small and the extrapolated value of $\sigma_S(82 \text{ K}) \approx 0.2 \text{ emu g}^{-1}$ (see the inset in Fig. 5) corresponds to the presence of only ~ 0.3 wt.% Ni in the sample.

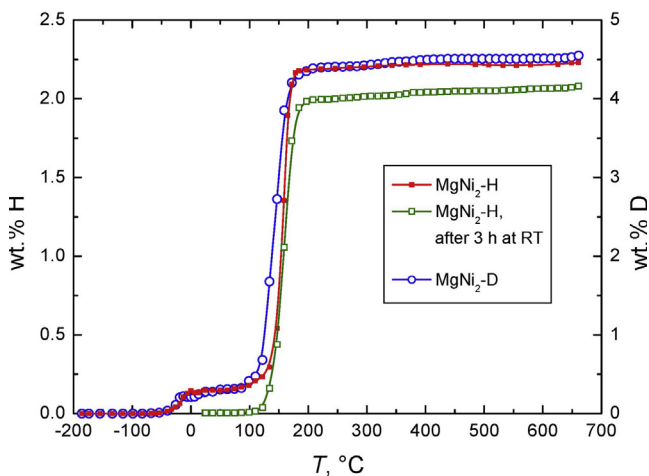


Fig. 4. Vacuum thermal desorption spectroscopy of the decomposition of the $\text{MgNi}_2\text{-H}$ sample (left scale) and $\text{MgNi}_2\text{-D}$ sample (right scale), measured during their heating at a rate of 20 °C min^{-1} in a pre-evacuated volume. The hydrogen content is expressed in the units of the mass ratio of the released hydrogen gas and the initial hydride sample.

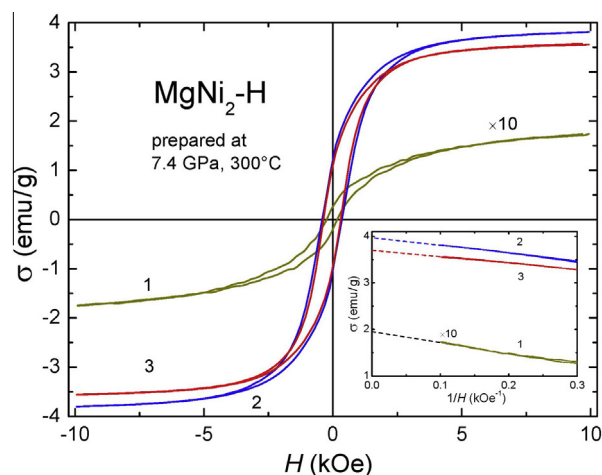


Fig. 5. Magnetization, σ , as a function of the applied magnetic field, H , for a 20 mg sample of the $\text{MgNi}_2\text{-H}$ sample in the “as-quenched” state (curve 1, $T = 82$ K) and after its 3 h exposure to room temperature resulted in the complete loss of hydrogen by the NiH phase (curve 2 measured at $T = 82$ K and curve 3 measured at $T = 295$ K). The field was varied from +10 to -10 kOe and backward at a constant rate of 1.2 kOe min^{-1} . The dashed lines in the inset show linear extrapolations of the experimental $\sigma(1/H)$ plots to $1/H = 0$.

As seen from Fig. 5, the magnetization of the $\text{MgNi}_2\text{-H}$ sample considerably increases after 3 h of annealing at room temperature because of the complete transformation of the NiH into Ni metal. Treating the experimental $\sigma(H)$ dependences in the same way as in the case of the virgin MgNi_2 alloy gives $\sigma_S^{\text{exp}}(82 \text{ K}) = 3.97 \text{ emu g}^{-1}$ and $\sigma_S^{\text{exp}}(295 \text{ K}) = 3.70 \text{ emu g}^{-1}$ and, correspondingly, $\sigma_S^{\text{exp}}(295 \text{ K})/\sigma_S^{\text{exp}}(82 \text{ K}) = 0.93$, which is close to $\sigma_S^{\text{Ni}}(295 \text{ K})/\sigma_S^{\text{Ni}}(82 \text{ K}) = 0.944$ of bulk Ni measured in Ref. [22]. The concentration of the Ni determined as $\sigma_S^{\text{exp}}/\sigma_S^{\text{Ni}}$ reaches $x_{\text{Ni}} \approx 6.8\text{--}7$ wt.%, which is ~ 4 wt.% larger than $x_{\text{Ni}} \approx 3$ wt.% in the starting MgNi_2 alloy. A calculated profile of the contribution from 7 wt.% NiH to the XRD pattern of the “as-quenched” $\text{MgNi}_2\text{-H}$ sample is shown in Fig. 3.

Nearly all peaks in the experimental diffraction pattern of the $\text{MgNi}_2\text{-H}$ sample, present due to the contribution from 7 wt.% NiH, can be indexed in an orthorhombic unit cell with $a \approx 4.55 \text{ \AA}$, $b \approx 4.69 \text{ \AA}$ and $c \approx 8.80 \text{ \AA}$. The measured values of the unit cell parameters agree with the results of Ref. [12]. However, in contrast with the data in Ref. [12], the actual symmetry of the orthorhombic unit cell of the trihydride MgNi_2H_x is face-centered orthorhombic and not a primitive one as proposed in Ref. [12]. The extinction symbol is found to be $F\text{---}$.

To derive the space group and the atomic structure of the orthorhombic phase, we started with the MoSi_2 -type structure (space group $I4/mmm$, No. 139) proposed for the tetragonal modification of the $\text{MgNi}_2\text{H}_{3.2}$ hydride in Ref. [11]. An orthorhombic distortion of this structure along the (110) axis allowed a satisfactory description of the observed splitting of the diffraction peaks and their intensities. The relations between the orthorhombic and tetragonal cells are: $a_{\text{orth}} \approx a_{\text{tetr}} \sqrt{2}$; $b_{\text{orth}} \approx a_{\text{tetr}} \sqrt{2}$; $c_{\text{orth}} \approx c_{\text{tetr}}$. In Fig. 3, the orthorhombic splitting is clearly seen, for example, for the $(200)_{\text{orth}}$ and $(020)_{\text{orth}}$ peaks, which appear at, respectively, 38.38° and 39.61° and stem from the $(110)_{\text{tetr}}$ peak of the tetragonal unit cell.

Profile refinement of the XRD diffraction pattern suggested formation of the orthorhombic crystal structure of the MgNi_2H_x hydride with space group $Fmmm$ (No. 69), giving the structural parameters presented in Table 2. Thus, the symmetry reduction to the space group $Pmmm$ (No. 47) suggested in Ref. [11] is not confirmed by the present refinement. Hydrogenation results in a volume expansion of 17.6% or 2.3 \AA^3 per at.H.

As can be seen from the difference spectrum shown in Fig. 3, the unidentified phase in the $\text{MgNi}_2\text{-H}$ sample mostly manifests itself by significant differences in the calculated and experimental intensities of diffraction lines in the angular range $37 < 2\theta < 47^\circ$. Small unidentified peaks are also observed at $2\theta = 53.7, 61.8, 69.7, 74.3$ and 75.3° . The secondary phase is different from those in the starting MgNi_2 alloy and its origin requires discussion.

Note in the first place that the MgNi_3 phase is absent in the hydrogenated sample; instead, this sample contains an additional 4 wt.% Ni compared to the starting alloy. The nickel concentration of 67.1 at.% in the MgNi_2 compound formed in the starting alloy lies well within the homogeneity region of $65 < X < 70$ at.% Ni of the $\text{MgNi}_2\text{H}_{\sim 3}$ hydrides synthesized in Ref. [11]. It is therefore unlikely that the extra Ni could precipitate from the nearly stoichiometric MgNi_2 compound in the course of its hydrogenation under a high hydrogen pressure. Most probably, the extra Ni resulted from the disproportionation of the MgNi_3 secondary phase present in the starting alloy and disappearing in the hydrogenated sample. Because of the thermodynamic instability of the intermetallic hydrides as related to the corresponding mixture of binary hydrides, disproportionation frequently occurs for many intermetallic compounds reacting with hydrogen gas, especially at high applied temperatures and hydrogen pressures.

Assuming a disproportionation reaction $\text{MgNi}_3 + (5/2)\text{H}_2 = \text{MgH}_2 + 3\text{NiH}$, the observed formation of the additional 4 wt.% Ni in the hydrogenated sample will require the presence of 4.5 wt.% MgNi_3 in the starting sample, which is consistent with its concentration of 2–4 wt.% MgNi_3 determined by XRD. The reaction will also produce about 0.6 wt.% MgH_2 . However, its contribution to the XRD pattern should be very small because of the low content of MgH_2 , small X-ray scattering length of Mg and because of the nearly amorphous structure of the MgH_2 precipitates usually formed in disproportionation reactions. The contribution from this MgH_2 to the total hydrogen content of the $\text{MgNi}_2\text{-H}$ sample should mostly compensate for the presence of 1–2 wt.% MgO, which does not react with hydrogen under the chosen synthesis conditions (XRD and thermal desorption analysis revealed no traces of interaction of MgO with hydrogen in a quenched sample of MgO powder exposed to a hydrogen pressure of 7.4 GPa at $T = 300^\circ\text{C}$ in an additional experiment).

Turning back to the unidentified phase in the $\text{MgNi}_2\text{-H}$ sample, we think it most likely that it is actually the MgNi_2H_x hydride with the same mean composition as the crystalline phase, but in the form of strongly deformed nanocrystalline grains containing many defects. Such a microstructure could result from the specific mechanism of the reconstructive transition of the MgNi_2 compound to the MgNi_2H_x hydride. This suggestion can indirectly be supported by the observation that the reverse transformation from MgNi_2H_x to MgNi_2 occurring on heating the hydrogenated sample in vacuum gives a sample with

strongly broadened diffraction lines. A very strong broadening of diffraction lines of the MgNi_2 compound after decomposing a $\text{MgNi}_2\text{H}_{3.2}$ hydride by heating to 500°C in a calorimeter was also observed in Ref. [11].

The assumption that the studied $\text{MgNi}_2\text{-H}$ sample can be considered as only consisting of NiH and a homogeneous MgNi_2H_x hydride is additionally confirmed by an analysis of the hydrogen balance. Decomposition of 7 wt.% of NiH after exposing the sample to room temperature should have decreased its hydrogen content by ~ 0.12 wt.% (hot extraction gave ~ 0.15 wt.% H, see Fig. 4). If the ~ 2.1 wt.% H remaining in the sample refers to $100 - 7 = 93$ wt.% of the MgNi_2H_x hydride, then this hydride contains ~ 2.26 wt.% H and this corresponds to the chemical formula $\text{MgNi}_2\text{H}_{3.2}$ in agreement with the results of Refs. [11,12].

3.4. The $\text{MgNi}_2\text{-D}$ sample

The XRD pattern of the $\text{MgNi}_2\text{-D}$ sample loaded with deuterium at 2.8 GPa and 300°C and quenched to the liquid N_2 temperature was very similar to that of the $\text{MgNi}_2\text{-H}$ sample synthesized at 7.4 GPa. The major phase was MgNi_2D_x with the same orthorhombic $Fmmm$ structure and virtually the same parameters of the unit cell as the $\text{MgNi}_2\text{H}_{3.2}$ phase (see Table 1). The sample also contained a few per cent of fcc NiD with $a = 3.72(1) \text{ \AA}$ and of the order of 10 wt.% of an unidentified phase similar to the unidentified hydride phase found in the $\text{MgNi}_2\text{-H}$ sample.

Thermal desorption analysis of ~ 5 mg of the $\text{MgNi}_2\text{-D}$ sample demonstrated that the decomposition kinetics and the total content of the hydrogen isotope of the MgNi_2D_x and NiD phases were similar to those of the MgNi_2H_x and NiH phases in the $\text{MgNi}_2\text{-H}$ sample (see Fig. 4). Measuring the magnetization of an ~ 20 mg portion of the $\text{MgNi}_2\text{-D}$ sample with NiD completely decomposed to Ni metal by a 3 h exposure to room temperature gave $\sigma(H)$ dependences similar to those of the $\text{MgNi}_2\text{-H}$ sample subjected to the same thermal treatment (see curves 2 and 3 in Fig. 5). The values of $\sigma_s^{\text{exp}}(82 \text{ K})$ and $\sigma_s^{\text{exp}}(295 \text{ K})$ corresponded to $\sim 6.8\text{--}7$ wt.% Ni in the partly outgassed $\text{MgNi}_2\text{-D}$ sample and therefore ~ 7 wt.% NiD in the “as-quenched” sample. In view of the close similarity in the phase compositions of the $\text{MgNi}_2\text{-D}$ and $\text{MgNi}_2\text{-H}$ samples, a consideration analogous to that in the previous section leads to the conclusion that both MgNi_2D_x phase and the unidentified phase have compositions close to $\text{MgNi}_2\text{D}_{3.2}$, the unidentified phase being a fine-grained and more inhomogeneous and distorted form of the crystalline $\text{MgNi}_2\text{D}_{3.2}$ deuteride.

Fig. 6 presents a TOF neutron diffraction pattern of the “as-quenched” $\text{MgNi}_2\text{-H}$ sample. The data are collected at $T = 100 \text{ K}$. When loading and cooling the sample in the nitrogen cryostat of the DN-2 neutron diffractometer, it stayed near room temperature for a few minutes, and NiD partly decomposed to Ni. Under the constraint that the total concentration of the NiD and Ni phases was 7 wt.%, a profile analysis of the experimental diffraction pattern gave 4 wt.% NiD and 3 wt.% Ni. The profiles calculated for these phases are shown at the bottom of Fig. 6.

The best fit of the neutron diffraction pattern was achieved assuming that D atoms fully occupy two types of sites, the $4b$ and $8f$ sites, which gives the total composition MgNi_2D_3 . The results of the refinements are presented in Table 2. The solid curve drawn through the experimental

Table 2. Results of profile analysis of the XRD patterns for the MgNi₂-H and MgNi₂-D samples ($T = 85$ K, Cu K_{α} radiation) and a neutron diffraction pattern for the MgNi₂-D sample ($T = 100$ K, TOF spectrum). The calculations are carried out for stoichiometric MgNi₂H₃ and MgNi₂D₃ structures described by the space group $Fm\bar{3}m$ (No. 69).

Compound	Atom	Position	X	Y	Z	B (\AA^{-2})
MgNi ₂ H ₃ $a = 4.553(4)$ $b = 4.686(4)$ $c = 8.796(6)$ \AA	Mg	4a	0	0	0	0.6
	Ni	8i	0	0	0.3189(8)	0.4
MgNi ₂ D ₃ $a = 4.552(5)$ $b = 4.690(5)$ $c = 8.796(7)$ \AA	Mg	4a	0	0	0	0.6
	Ni	8i	0	0	0.30(2)	0.4
	D1	4b	0	0	1/2	0.8
	D2	8f	1/4	1/4	1/4	0.8

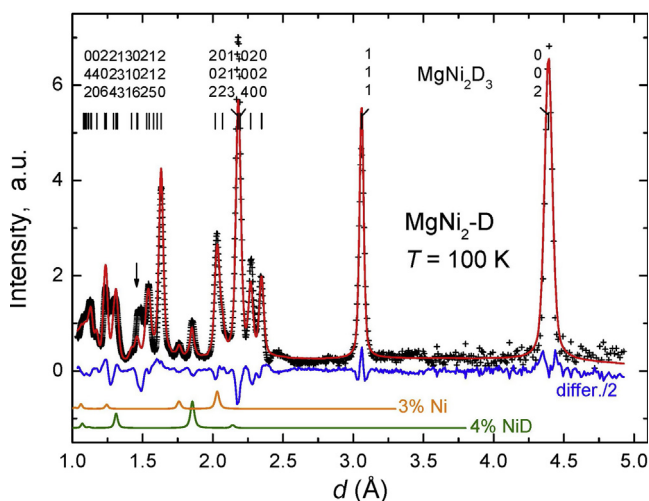


Fig. 6. Neutron diffraction pattern of the MgNi₂-D sample prepared at a deuterium pressure of 2.8 GPa and a temperature of 300 °C (experimental points and their profile fit shown by the solid curve), the calculated contributions from the 4 wt.% NiD and 3 wt.% Ni impurities (two curves at the bottom) and the difference between the calculated and experimental profiles (scale 1/2; the curve is labeled “differ./2”). The pattern is collected at 100 K with the DN-2 TOF neutron diffractometer at JINR in Dubna. $R_{wp} = 27.4\%$, $R_p = 20.9\%$, $\chi^2 = 21.5$.

points in Fig. 6 shows the sum of the calculated contributions from the crystalline part of the MgNi₂D_x deuteride and the major secondary phases, NiD and Ni.

In view of the large amount of the unidentified phase in the MgNi₂-D sample, the profile fit of the experimental diffraction pattern is rather semiquantitative in character. Although no experimental peaks are left unindexed, the intensities of some peaks are not well reproduced. The largest and unresolvable difference between the calculation and experiment is observed near the interplanar distance $d = 1.46$ \AA (marked by the vertical arrow in Fig. 6). Nevertheless, the quality of the refinement is sufficient to uniquely determine the positions of the D atoms in the crystal structure of MgNi₂D₃ because these are the only interstitial sites in the metal lattice of the deuteride that match the constraints well established for the hydrides of intermetallic compounds such as the “rule of 2 \AA” and Me–H distances of $(r_{Me} + 0.4)$ \AA [7,25].

The crystal structure of MgNi₂D₃ is shown in Fig. 7. The position D1 of a deuterium atom is coordinated by an octahedron of Mg₄Ni₂ (4 Mg–D1 = 2.275 \AA; 2 Ni–D1 = 1.759 \AA). In contrast, D2 atoms are not surrounded

by Mg atoms and are centering buckled squares of Ni₄, creating deformed planar networks located at $z = 1/4$ and $z = 3/4$ of the structure, with an Ni–D2 distance of 1.691 \AA.

The closest interatomic metal–H distances in the structure agree well with the typical values observed in the Mg- and Ni-containing hydrides (1.97–2.33 \AA for Mg–D and 1.52–1.73 for Ni–D, in La₂MgNi₉D₁₃ [7]). The shortest D–D distance of 2.30 \AA complies with the “rule of 2 \AA” [25].

According to Refs. [11,12], the MgNi₂H_{3,2} hydride can exist in two modifications, the orthorhombic one studied in the present work as well as a related tetragonal modification (space group $I4/m\bar{3}m$ (No. 139), $a = 3.27(3)$ \AA, $c = 8.78(9)$ \AA) with a higher symmetry. Removing the orthorhombic distortion of the described $Fm\bar{3}m$ structure of the MgNi₂D₃ deuteride, we can obtain the positions of H atoms in the unit cell of this tetragonal hydride. These will be two positions: H1 (2b) ($00\frac{1}{2}$) filling an Mg₄Ni₂ octahedron, and H2 (4d) ($0\frac{1}{2}\frac{1}{4}$) located in the Ni net and having Ni₂ coordination.

3.5. Electronic structures of MgNi₂ and MgNi₂H₃

3.5.1. Methodology and crystal structures

The calculations reported in this work are based on the density functional theory (DFT). They have been performed using the projector augmented wave method

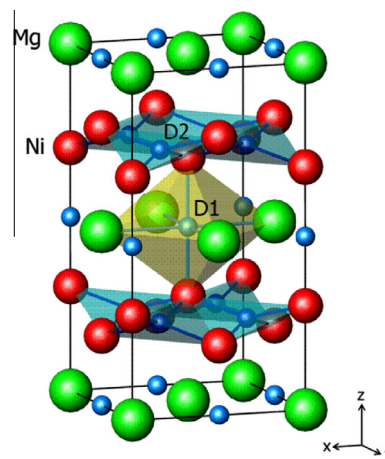


Fig. 7. The crystal structure of MgNi₂D₃. D1 in Mg₄Ni₂ octahedron and buckled Ni nets formed from centered by D2 atoms deformed Ni₄ squares are shown.

(PAW) [26], implemented in the Vienna Ab initio Simulation Package (VASP) [27,28]. The exchange-correlation energy of electrons is described in the generalized gradient approximation (GGA) using the Perdew–Burke–Ernzerhof functional parametrization [29]. Semi-core p electrons of Mg and Ni have been considered. After necessary tests to control the stability of the energy differences between phases, the energy cut-off for the PAWs was set to

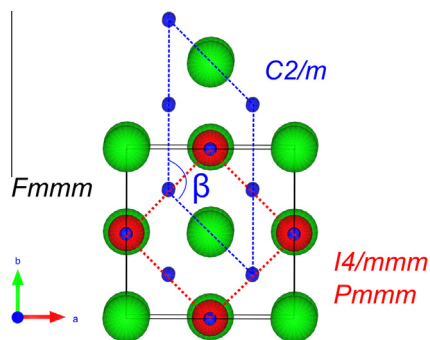


Fig. 8. The $I4/mmm$, $Pmmm$ and $C2/m$ symmetries are deduced from the $Fm\bar{3}m$ symmetry.

800 eV. Charge transfers have been computed using Bader's prescription [30,31]. As a first try, we have intentionally kept the $Fm\bar{3}m$ space group whilst relaxing the crystal structure (volume and internal parameters). As a consequence, a spontaneous lowering of the symmetry was not possible. The introduction of 3-H in the metallic matrix leads to an increase of 20.75% of the host cell volume. Moreover, a calculation initiated with the experimental orthorhombic symmetry with an additional relaxation allowing the cell shape to be free has converged to a tetragonal symmetry with $a' = b'$ into the $I4/mmm$ space group. Several orthorhombic crystal structures have been tested, such as the one reported by Okada's group in $Pmmm$ [11]. Reducing the symmetry by adding a monoclinic tilt ($\sim 1^\circ$) leading to a β angle of $\sim 134^\circ$ allows the $C2/m$ space group. Tested crystal structures are represented on Fig. 8 and converged results are summarized in Table 3. The zero-point energy (ZPE) has been extracted from the phonon calculations, which have been done by the supercell approach ($2 \times 2 \times 2$) using the Phonopy code [32].

3.5.2. Analysis of the electronic structure

The total DOS of the $MgNi_2$ host compound plotted in Fig. 9 is mainly associated with Ni d -states hybridized with

Table 3. Relaxed crystal structure parameters and gross/ZPE-corrected heat of formation at 0 K of $MgNi_2H_3$ for several candidate structures.

Space group	$Fm\bar{3}m$ (69)	$I4/mmm$ (139)	$Pmmm$ (47)	$C2/m$ (12)
a (Å)	4.7236	3.2970	3.3133	4.6562
b (Å)	4.5846	–	3.3034	8.8394
c (Å)	8.8590	8.8234	8.7700	7.4320
β				116.27°
Mg	4a	2a	1a, 1h	2d
Ni	8i; $z = 0.3167$	4e; $z = 0.3159$	2q; $z = 0.3150$, 2t; $z = 0.1849$	4h; $y = 0.1838$
H1	4b	2b	1c, 1f	2c
H2	8f	4d	2r $z = 0.2490$, 2s $z = 0.7490$	4g; $y = 0.2402$
ΔH (kJ/mol- H_2)	–34.10	–34.72	–35.17	–34.83
ΔH^{corr} (kJ/mol- H_2)	–26.15	–27.15	–27.56	–27.69

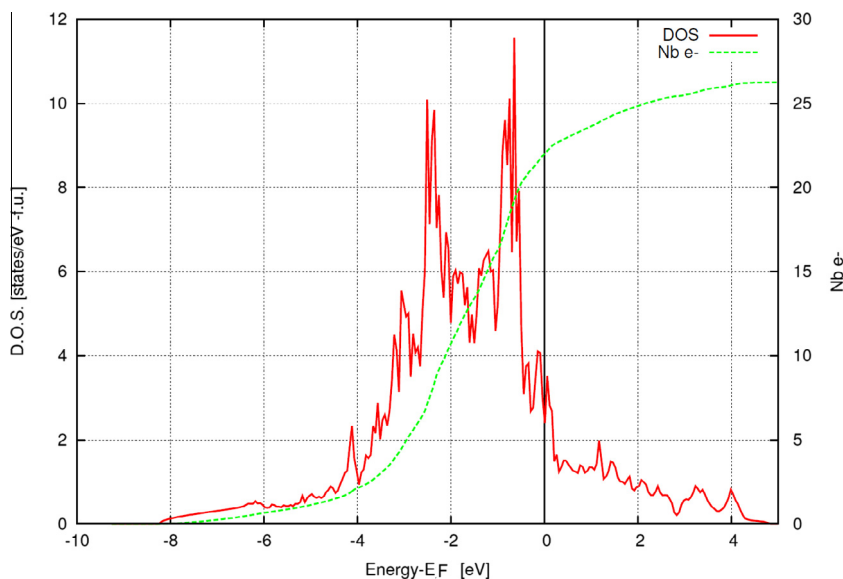


Fig. 9. Total DOS of $MgNi_2$ (C36-type structure), left vertical scale, and number of electrons, right vertical scale. The Fermi energy, E_F , is chosen as the origin of energies.

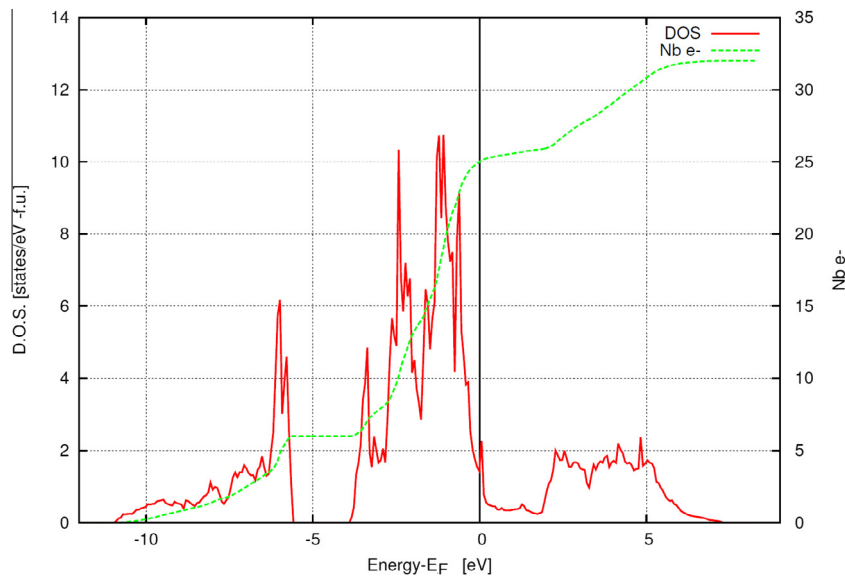


Fig. 10. Total DOS of MgNi_2H_3 ($Fmmm$), left vertical scale, and number of electrons, right vertical scale. The Fermi energy, E_F , is chosen as the origin of energies.

Ni s - and p -states and Mg s - and p -states. An electronic charge transfer from Mg to Ni occurs, with respective final charges of $-1.51e^-$ and $+0.75e^-$, which explains the almost filled $3d$ -states of Ni. The compound is metallic and spin-polarized calculations lead to a paramagnetic state, in agreement with the magnetization measurements [20].

The total DOS of MgNi_2H_3 calculated in the $Fmmm$ space group and plotted in Fig. 10 shows three main structures that can be identified with the help of the partial wave analysis of the DOS (PDOS) presented in Figs. 10–13. The insertion of hydrogen leads to the low-energy structure of the DOS extending from around -11 to -6 eV, which is mainly due to Ni $3d$, H s bonds, with smaller Ni s , p and Mg s , p contributions. Calculations of partial DOS for H1 and H2 show a slightly stronger interaction of Mg with H2 atoms as expected from the crystal structure. The bonding structure of PDOS of Fig. 13 is observed at slightly lower energy, around -7 eV, for H2 (at the center of the Ni_4 square) as compared to H1 (filling the Mg_4Ni_2 octahedron). The low-energy bonding structure is separated by an energy gap, located between -5.5 and -3.5 eV, from the

main Ni $3d$ structure. This structure is slightly, 0.5 eV, narrower for the hydride than for the intermetallic due to both lattice expansion and energy lowering of the Ni d -states involved in the Ni–H bonds. The hydride is found to be metallic with a DOS at the Fermi energy of 1.57 states/eV-f.u. lower than that of MgNi_2 , 2.2 states/eV-f.u. associated with a further filling of the Ni $3d$ -states in the hydride. Above the Fermi level of the hydride, the structure extending up to 6 eV is associated with antibonding H-metal states. Bader's calculation indicated a charge transfer from Mg ($-1.55e^-$) to Ni ($+0.18e^-$), H1 ($+0.6e^-$) and H2 ($+0.3e^-$).

Fig. 14 shows the electron localization function (ELF) plots in several planes. The more electron localized areas are around the H atoms, mainly because of the electronic charge transfer from the metallic elements. The hydride is clearly not a complex hydride as the Mg_2NiH_4 one, but rather an interstitial-type hydride. According to the crystallographic structure, the H1 atom is located at the center of the Mg_4Ni_2 octahedra, with a shorter distance between H–Ni than between H–Mg, as represented by the bond

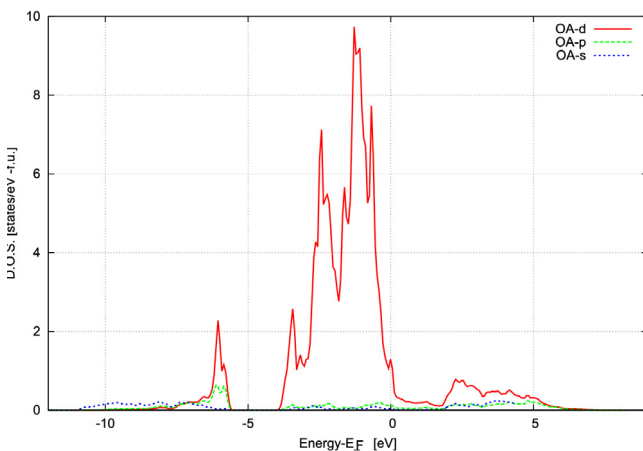


Fig. 11. Partial DOS for 2-Ni in MgNi_2H_3 .

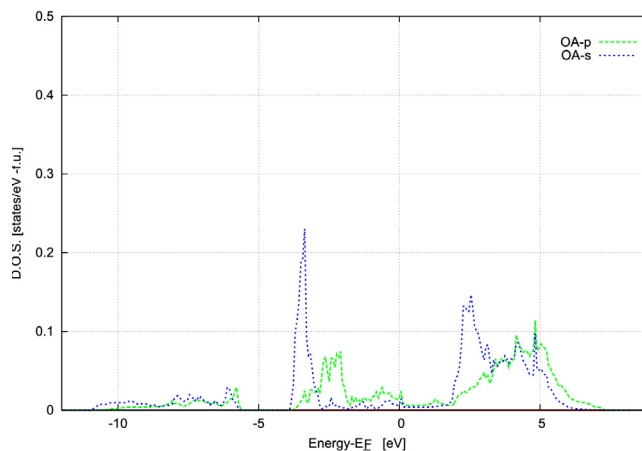


Fig. 12. Partial DOS for Mg in MgNi_2H_3 .

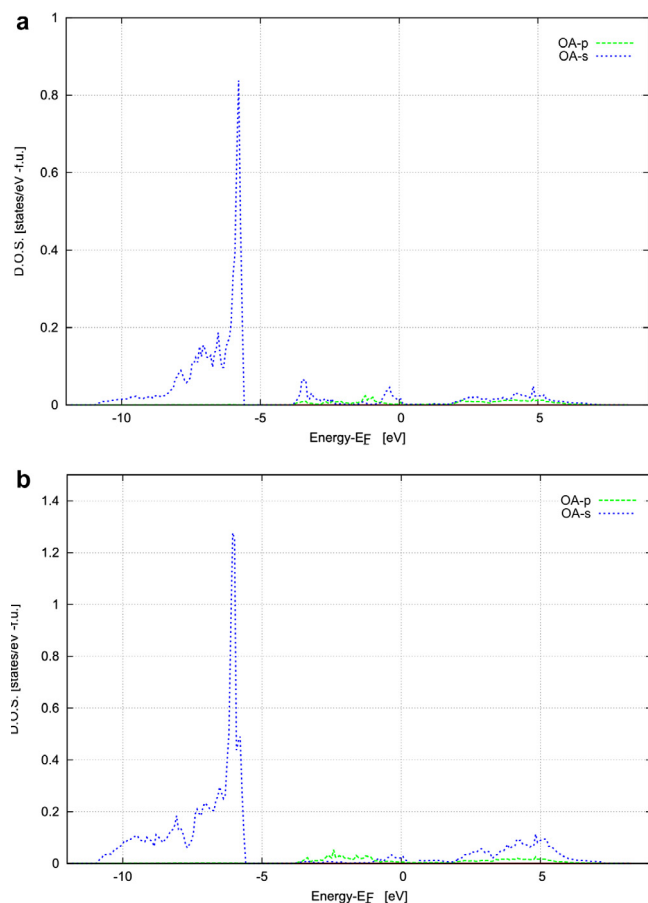


Fig. 13. Partial DOS for hydrogen H1 (a) and 2-H2 (b).

between H and Ni, whereas H2 is at the center of buckled squares Ni_4 .

3.5.3. Phase and lattice stabilities

In all cases, DFT and phonon calculations have been performed at 0 K for equilibrium relaxed structures. Phonon calculations of all products and reactants allowed their band phonon plot and the zero-point-energy correction at $T = 0$ K (ZPE) to be obtained. Table 3 presents the calculated heats of formation of compounds and the heat of the reaction: $\text{MgNi}_2 + 3/2 \text{H}_2 \rightarrow \text{MgNi}_2\text{H}_3$.

Irrespective of the space group considered, the ZPE corrected enthalpy of formation of MgNi_2H_3 is about -30 kJ/mol- H_2 , which is consistent with the stability of the hydride at normal conditions and its decomposition above 100 °C. Whereas the orthorhombic $Fm\bar{3}m$ (69) description is the least stable structure at 0 K, and converges to the more stable tetragonal $I4/m\bar{3}m$ (139) one, the calculated orthorhombic $Pn\bar{3}m$ (47) or monoclinic $C2/m$ (12) structures are both slightly lower in energy.

However, the phonon dispersion curves present negative frequencies for all structures (see Fig. 15a) except for the lowest-symmetry $C2/m$ description (Fig. 15b). This means that all other structures are mechanically unstable at 0 K. We note that these structures may become stabilized by increasing the temperature. Since the $Fm\bar{3}m$ structure has been observed at 100 K, it is possible that a phase transition occurs leading to a lower-symmetry $C2/m$ at low temperature. Some additional neutron measurements at 4 K may shed light on this hypothesis.

The partial phonon DOS for the $C2/m$ structure are plotted in Fig. 15c. They show a dominant contribution of the heaviest Ni atom at the lowest frequencies coupled with Mg for some modes. The optical branches, at higher frequencies, are associated with the lighter H atom contribution (the modes of the two sites H1 and H2 are distinct and are not coupled).

4. Discussion and conclusions

Ti_2PdH_2 and Ti_2PdH_3 hydrides with MoSi_2 -related tetragonal structures have previously been studied experimentally and theoretically [33,34]. The hydrides Ti_2PdH_2 and Ti_2PdH_3 crystallize with tetragonal unit cells having high c/a ratios of 3.6–3.8. These studies showed that H atoms occupy tetrahedral Ti_4 and octahedral Ti_5Pd sites.

Hydrogen-induced phase transformation from the $C36$ Laves-type to MoSi_2 -related structure takes place during the hydrogenation of MgNi_2 to form a trihydride MgNi_2H_3 .

In the orthorhombic $\text{MgNi}_2\text{H}(\text{D})_3$, the c/a (c/b) ratios are much smaller, 2.6–2.7, with hydride-forming Mg filling the Mo sites while Ni occupies the Si sites. This contrasts to the situation with the Ti_2Pd -based hydrides, where the hydride-forming Ti fills the Si sites while Pd occupies the Mo sites. These two major differences between the

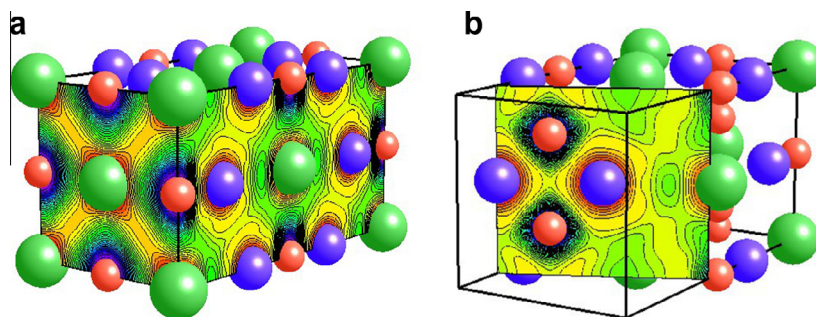


Fig. 14. Electron localization function images in MgNi_2H_3 . Atoms are represented by spheres: Mg (green), Ni (blue) and H (red). Warm color (red) areas indicate nonlocalized electrons (probability of presence close to 0), whereas cold colors (blue) represent strong localization (probability of presence close to 1), green areas correspond to a probability of 0.5, characteristic of metallic behavior. (a) Shows Ni–H1 bonding; (b) shows Ni–H2 bonding in buckled Ni–H–Ni–H nets of MgNi_2H_3 . (For interpretation of the references to colour in this figure legend, the reader is referred to the web version of this article.)

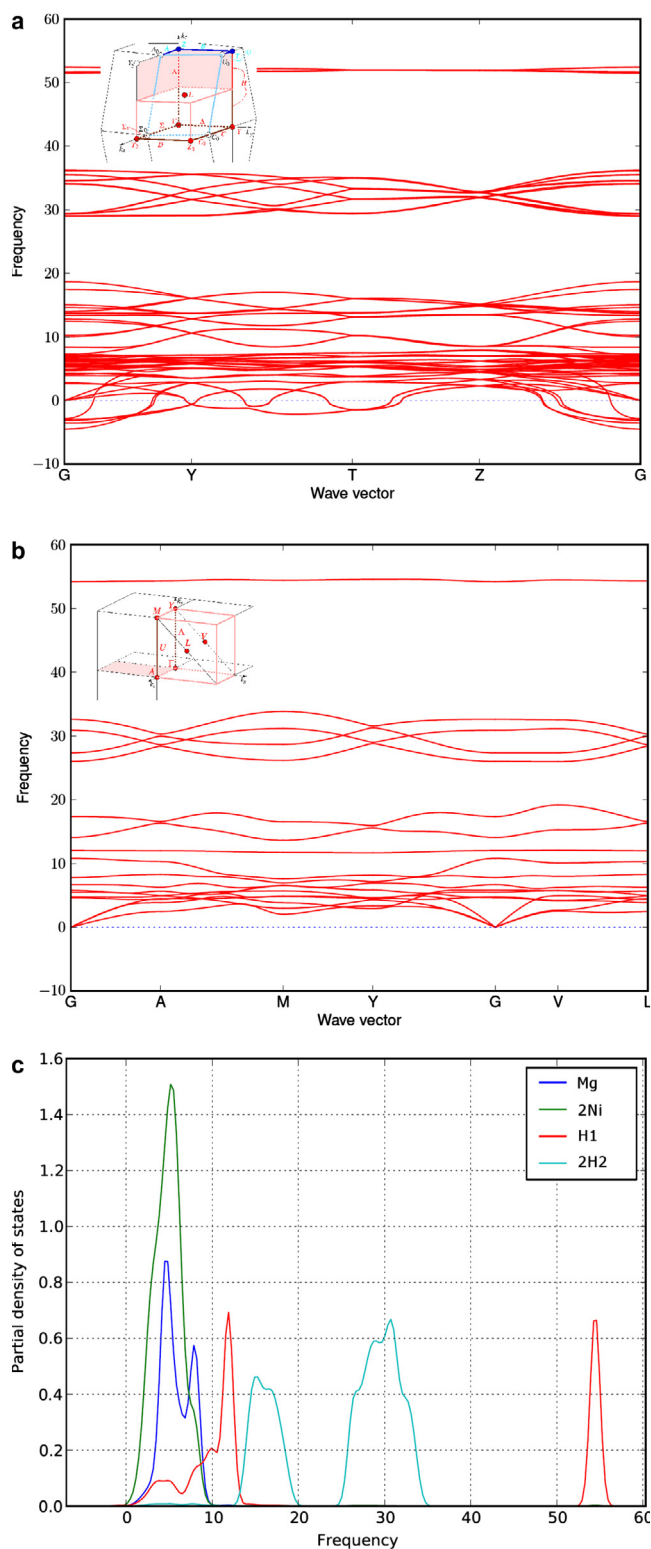


Fig. 15. Phonon dispersion curves of MgNi_2H_3 calculated for the $Fmmm$ (a) and $C2/m$ structures (b), and partial phonon DOS for this latter structure (c). Frequencies are in THz.

crystallographic aspects of the formation of MgNi_2H_3 and $\text{Ti}_2\text{PdH}_{2-3}$ hydrides and their chemistry result in the formation of different types of structures for MgNi_2H_3 as compared to Ti_2PdH_2 and Ti_2PdH_3 .

MgNi_2 is found to form an orthorhombic hydride phase under high hydrogen pressures, 2.8–7.4 GPa, and a

temperature of 300 °C. The crystallographic data for the studied hydride well agree with the reference data (where only the metrics of the unit cell was described). However, the present study is the first to report on the atomic structure of the trihydride MgNi_2D_3 and formation of an ordered type of the hydrogen sublattice. Interestingly, the arrangement of the D atoms within the unit cell is symmetric with respect to an a – b axes exchange, and therefore does not explain the occurrence of the orthorhombic distortion.

In the present study, we have not observed the formation of the tetragonal phase MgNi_2H_3 . Formation of orthorhombic or tetragonal structures has been experimentally confirmed to occur at various Mg/Ni ratios, in the area enriched by Mg (tetragonal hydride), or at stoichiometric MgNi_2 and overstoichiometric MgNi_{2+x} compositions containing 67–70 at.% Ni.

Calculations of the electronic structure show that the total energies of the orthorhombic, tetragonal or monoclinic possible structures of the MgNi_2H_3 hydride are very close to each other. Although comparison of the heats of formation indicates that the monoclinic modification is slightly more stable, further work needs to be done to determine the stability ranges of these hydride phases, which are affected by the Mg/Ni ratios and applied P – T synthesis and quenching conditions. The phonon calculation suggests that the monoclinic structure should be the only mechanically stable one at 0 K. Additional measurements at low temperature might confirm if any symmetry lowering occurs from the $Fmmm$ one when cooling down from 100 K.

Finally, electronic structure studies show that the bonding mechanism between the hydrogen atoms and metal atoms in MgNi_2H_3 is dominated by the formation of covalent bonds between Ni and H and a charge transfer from Mg to H1, leading to a significant degree of ionic bonding between Mg (effective positive charge $1.55e^-$) and H1 (effective negative charge $-0.6e^-$). Ni and H2 also receive electrons from Mg, but the effect is much lower as compared to the $\text{Mg} \rightarrow \text{H1}$ transfer.

Covalent Ni–H bonding has previously been found in $\text{CeNi}_3\text{H}_{2.7}$ and $\text{Ce}_2\text{Ni}_7\text{H}_{4.5}$ [35]. Both CeNi-based intermetallic hydrides contain spatial Ni–H–Ni–H nets covalently binding Ni and H atoms, which are similar to the one observed in the present study. Thus, covalent bonding between nickel and hydrogen should be considered as an important feature allowing formation of stable Ni-based intermetallic hydrides.

Acknowledgements

This work was supported by ERA Net Russia FP7 program (Project NOVELMAG # 225) and a grant by the Program “Elementary Particle Physics, Fundamental Nuclear Physics and Nuclear Technologies” of the Russian Academy of Sciences. We would like to thank IDRIS (Institut du Développement et des Ressources en Informatique Scientifique) for providing access to the high-performance computing (HPC) resources of GENCI (Grand Equipement National de Calcul Intensif) under Project Nos. 096175 and 90189 for the electronic structure work presented in this paper.

References

- [1] S. Løken, J.K. Solberg, J.P. Maehlen, R.V. Denys, M.V. Lototsky, B.P. Tarasov, et al., *J. Alloys Compd.* 446–447 (2007) 114.

- [2] A.A. Poletaev, R.V. Denys, J.P. Maehlen, J.K. Solberg, B.P. Tarasov, V.A. Yartys, *Int. J. Hydrogen Energy* 37 (2012) 3548.
- [3] R.V. Denys, A.B. Riabov, V.A. Yartys, Masashi Sato, R.G. Delaplane, *J. Solid State Chem.* 181 (4) (2008) 812.
- [4] R.V. Denys, V.A. Yartys, *J. Alloys Compd.* 509 (Supplement 2) (2011) S540.
- [5] C.C. Nwakwuo, Th. Holm, R.V. Denys, Weikang Hu, J.P. Maehlen, J.K. Solberg, et al., *J. Alloys Compd.* 555 (2013) 201.
- [6] Wei-Kang Hu, R.V. Denys, C. Nwakwuo, Th. Holm, J.P. Maehlen, J.K. Solberg, et al., *Electrochim. Acta* 96 (2013) 27.
- [7] R.V. Denys, V.A. Yartys, C.J. Webb, *Inor. Chem.* 51 (7) (2012) 4231.
- [8] R.V. Denys, V.A. Yartys, C.J. Webb, MH2012, Kyoto, Japan, 21–26 October 2012, Collected Abstracts: 92.
- [9] T.B. Massalski (Ed.), *ASM Handbook, Alloy Phase Diagrams*, vol. 3, ASM International, Materials Park, OH, 1992.
- [10] Y. Komura, K. Tokunaga, *Acta Cryst.* B36 (7) (1980) 1548.
- [11] R. Kataoka, Y. Goto, A. Kamegawa, H. Takamura, M. Okada, *Mater. Trans.* 47 (8) (2006) 1957.
- [12] R. Kataoka, A. Kamegawa, H. Takamura, M. Okada, *Mater. Trans.* 50 (5) (2009) 1179.
- [13] L.G. Khvostantsev, V.N. Slesarev, V.V. Brazhkin, *High Pressure Res.* 24 (3) (2004) 371.
- [14] V.E. Antonov, *J. Alloys Compd.* 2002 (330–332) (2002) 110.
- [15] V.E. Antonov, A.I. Davydov, V.K. Fedotov, A.S. Ivanov, A.I. Kolesnikov, M.A. Kuzovnikov, *Phys. Rev. B* 80 (2009), 134302-1.
- [16] I.O. Bashkin, V.E. Antonov, A.V. Bazhenov, I.K. Bdikin, D.N. Borisenko, E.P. Krinichnaya, et al., *JETP Lett.* 79 (5) (2004) 226.
- [17] A.C. Larson, R.B. von Dreele, *General structure analysis system (GSAS)*, LANSCE, MS-H, vol. 805, 1994; V.B. Zlokazov, V.V. Chernyshev, *J. Appl. Cryst.* 25 (3) (1992) 447.
- [18] Web Elements Periodic Table, <http://www.webelements.com/nickel/crystal_structure.html>.
- [19] R. Kannan, M.S. Seehra, *Phys. Rev. B* 35 (13) (1987) 6847.
- [20] G. Liu, S. Xi, G. Ran, K. Zuo, P. Li, J. Zhou, *J. Alloys Compd.* 448 (1–2) (2008) 206.
- [21] K.H.J. Buschow, *Solid State Commun.* 17 (7) (1975) 891.
- [22] J. Crangle, G.M. Goodman, *Proc. R. Soc. Lond. A* 321 (1971) 477.
- [23] C.P. Bean, I.S. Jacobs, *J. Appl. Phys.* 27 (12) (1956) 1448.
- [24] V.E. Antonov, I.T. Belash, O.V. Zharikov, A.V. Palnichenko, *Phys. Status Solidi (b)* 142 (1987) K155.
- [25] V.A. Yartys, V.V. Burnasheva, K.N. Semenenko, *Russ. Chem. Rev.* 52 (4) (1983) 299.
- [26] P.E. Blöchl, *Phys. Rev. B* 50 (1994) 17953.
- [27] G. Kresse, J. Furthmüller, *Phys. Rev. B* 54 (1996) 11169.
- [28] G. Kresse, D. Joubert, *Phys. Rev. B* 59 (1999) 1758.
- [29] J.P. Perdew, K. Burke, M. Ernzerhof, *Phys. Rev. Lett.* 78 (1997) 1396.
- [30] R.F.W. Bader, N. York (Eds.), *Atoms in Molecules. A Quantum Theory*, Oxford University Press, Oxford, 1990.
- [31] G. Henkelman, A. Arnaldsson, H. Jónsson, *Comput. Mater. Sci.* 36 (2006) 354.
- [32] A. Togo, F. Oba, I. Tanaka, *Phys. Rev. B* 78 (2008) 134106.
- [33] A.J. Maeland, G.G. Libowitz, *J. Less Common Met.* 74 (1980) 295.
- [34] Xing-Qiu Chen, C.L. Fu, J.R. Morris, *Intermetallics* 18 (2010) 998.
- [35] V.A. Yartys, Ponniah Vajeeston, A.B. Riabov, Ponniah Ravindran, R.V. Denys, J.P. Maehlen, R.G. Delaplane, H. Fjellvåg, *Z. Kristallog.* 223 (10) (2008) 674.